Monthly Notices
of the
ROYAL ASTRONOMICAL SOCIETY

MNRAS **459,** 4485–4498 (2016)
Advance Access publication 2016 April 17

doi:10.1093/mnras/stw896

Ionized gas kinematics within the inner kiloparsec of the Seyfert galaxy NGC 1365

Davide Lena,[1,2,3★] Andrew Robinson,[1] Thaisa Storchi-Bergmann,[4] Guilherme S. Couto,[4] Allan Schnorr-Müller[5,6] and Rogemar A. Riffel[7]

[1]*School of Physics and Astronomy, Rochester Institute of Technology, 84 Lomb Memorial Drive, Rochester, NY 14623-5603, USA*
[2]*SRON, Netherlands Institute for Space Research, Sorbonnelaan 2, NL-3584 CA Utrecht, the Netherlands*
[3]*Department of Astrophysics/IMAPP, Radboud University, Nijmegen, PO Box 9010, NL-6500 GL Nijmegen, the Netherlands*
[4]*Instituto de Física, Universidade Federal do Rio Grande do Sul, 91501-970, Porto Alegre, Brazil*
[5]*Max-Planck-Institut für extraterrestrische Physik, Giessenbachstr. 1, D-85741, Garching, Germany*
[6]*CAPES Foundation, Ministry of Education of Brazil, 70040-020, Brasilia, Brazil*
[7]*Universidade Federal de Santa Maria, Departamento de Física, 97105-900, Santa Maria, RS, Brazil*

Accepted 2016 April 14. Received 2016 April 13; in original form 2015 September 9

ABSTRACT

We observed the nuclear region of the galaxy NGC 1365 with the integral field unit of the Gemini Multi Object Spectrograph mounted on the GEMINI-South telescope. The field of view covers 13 × 6 arcsec^2(1173 × 541 pc^2) centred on the nucleus, at a spatial resolution of 52 pc. The spectral coverage extends from 5600 to 7000 Å, at a spectral resolution R = 1918. NGC 1365 hosts a Seyfert 1.8 nucleus, and exhibits a prominent bar extending out to 100 arcsec (9 kpc) from the nucleus. The field of view lies within the inner Lindblad resonance. Within this region, we found that the kinematics of the ionized gas (as traced by [O I], [N II], Hα, and [S II]) is consistent with rotation in the large-scale plane of the galaxy. While rotation dominates the kinematics, there is also evidence for a fan-shaped outflow, as found in other studies based on the [O III] emission lines. Although evidence for gas inflowing along nuclear spirals has been found in a few barred galaxies, we find no obvious signs of such features in the inner kiloparsec of NGC 1365. However, the emission lines exhibit a puzzling asymmetry that could originate from gas which is slower than the gas responsible for the bulk of the narrow-line emission. We speculate that it could be tracing gas which lost angular momentum, and is slowly migrating from the inner Lindblad resonance towards the nucleus of the galaxy.

Key words: black hole physics – galaxies: active – galaxies: individual: NGC 1365 – galaxies: kinematics and dynamics – galaxies: nuclei – galaxies: Seyfert.

1 INTRODUCTION

The powerful non-stellar radiation observed in active galactic nuclei (AGNs) originates from gas accretion on to a supermassive black hole (SMBH; e.g. Lynden-Bell 1969; Soltan 1982). Accretion rates as low as 10^{-3} M$_\odot$ yr^{-1} are sufficient to reproduce the luminosity of local AGNs; however, despite the large amounts of gas present in galaxies, only 43 per cent of them are active (Ho 2008). Gas transfer from kpc scales down to sub-pc distances from the SMBH is, at the time of writing, a lively research topic. Reviews of the subject have been presented by Shlosman, Begelman & Frank (1990), Knapen (2005), Jogee (2006), and Alexander & Hickox (2012).

Theoretical work (e.g. Athanassoula 1992; Hopkins & Quataert 2010; Emsellem et al. 2015) and observations (e.g. García-Burillo et al. 2005) show that different mechanisms are efficient in the removal of gas angular momentum at different scales. Torques due to kpc-scale bars, or to interactions and mergers, are efficient at channelling gas from several kpc down to the inner few 100 pc. When a bar is present, gas stalls and accumulates at the inner Lindblad resonance resulting in rings of gas (e.g. Jogee et al. 2001) or star formation regions (e.g. Pérez-Ramírez et al. 2000). Gas might then be funnelled within a few parsec from the SMBH, or even closer, by nuclear bars, nuclear spirals (e.g. Hopkins & Quataert 2010), or because of dynamical friction (Jogee, Kenney & Smith 1999) and viscosity (Bekki 2000).

When a reservoir of gas is present in the nuclear region of an active galaxy, then an outflow may take place (e.g. Crenshaw, Kraemer & George 2003). Simulations suggest that AGN feedback has a crucial role in the evolution of the host galaxy (e.g. Di Matteo, Springel & Hernquist 2005); however the modelling of the AGN physics is

★E-mail: d.lena@sron.nl

© 2016 The Authors
Published by Oxford University Press on behalf of the Royal Astronomical Society

Downloaded from http://mnras.oxfordjournals.org/ at Universidade Federal do Rio Grande do Sul on October 26, 2016

still simplistic and robust observational constraints are still far from being set.

Kinematical features consistent with gas inflows and/or outflows on scales of 10–100 pc have been observed in a number of nearby galaxies (e.g. Fathi et al. 2006; Storchi-Bergmann et al. 2007; Riffel et al. 2008; Müller Sánchez et al. 2009; Schnorr-Müller et al. 2011, 2014a,b; García-Burillo & Combes 2012; Combes et al. 2014; Davies et al. 2014; Lena et al. 2015; Smajić et al. 2015; Scharwächter et al. 2015; Luo et al. 2016). However, a clear picture of the chain of events which ultimately feeds the AGN is yet to be established. How much of the accreted rest-mass energy is transferred to the interstellar medium through the outflows is still in the process of being determined.

Here we present a study of the ionized gas kinematics in the nuclear region of NGC 1365, one of the most extensively observed galaxies in the Southern hemisphere (see Lindblad 1999 for a detailed review of the early work). This is part of an ongoing study aimed at identifying correlations between the circum-nuclear gas kinematics and the SMBH accretion rate.

NGC 1365 is an archetypal barred galaxy, classified as SB(s)b by de Vaucouleurs et al. (1991). Jones & Jones (1980) identify the galaxy as a member of the Fornax cluster. It is known to host a Seyfert-like AGN which is classified as Seyfert 1.8 by Véron-Cetty & Véron (2006). The nuclear region exhibits signatures of both star formation and an AGN. Evidence that star formation plays a major role in the nucleus of the galaxy was, perhaps, first identified by Morgan (1958) who reported the presence of 'hot spots', i.e. bright H II regions. More recently, the coexistence of AGN and stellar photoionization, in the vicinity of the nucleus, has been nicely mapped with integral field observations by Sharp & Bland-Hawthorn (2010).

Signs of nuclear activity have been identified mainly at X-ray and optical wavelengths: Iyomoto et al. (1997) observe a strong FeK emission line, and a point-like hard X-ray source consistent, in position, with the optical nucleus; a power-law component was judged necessary to perform a satisfactory fit to nuclear X-ray spectra in Komossa & Schulz (1998). Risaliti et al. (2005) report on extreme X-ray variability of the hard X-ray continuum. This was later interpreted as the result of variations in the distribution of discrete absorbers along the line of sight (e.g. Braito et al. 2014, and references therein). Such findings lend support to the hypothesis that the hard X-ray emission in the nucleus of NGC 1365 is a genuine AGN signature. The recent study of Nardini et al. (2015), which is based on data from the Chandra High Energy Transmission Grating, reveals a rich spectrum of soft X-ray emission lines from photoionized gas in the immediate vicinity of the AGN. They show evidence of line broadening, outflow, and possibly inflows, with velocities of the order of 1000 km s^{-1}.

Optical spectroscopy revealed the presence of broad Balmer emission lines, narrow-line ratios typical of AGNs (e.g. Veron et al. 1980; Edmunds & Pagel 1982; Schulz et al. 1999), and the presence of [Ne V] and He II (Phillips & Frogel 1980) indicating photoionization by a hard extreme-UV continuum, as is characteristic of AGNs. Fabry–Perot interferometry and narrow-band imaging showed a fan-shaped [O III]λ5007 emission region extending about 10 arcsec (≈1 kpc) south-eastward of the nucleus (Edmunds, Taylor & Turtle 1988; Storchi-Bergmann & Bonatto 1991; Kristen et al. 1997).

Alonso-Herrero et al. (2012) present an infrared study of the inner 5 kpc. They infer that most of the star formation within the inner Lindblad resonance ($r \approx 30$ arcsec, or 2.7 kpc, Lindblad, Lindblad & Athanassoula 1996b) takes place within obscured regions, in a nuclear star-forming ring of radius ≈1 kpc. Furthermore, they propose that the photometric and spectral emission can be reproduced with a model including a torus with outer radius $r_o \approx 5$ pc, opening angle $\sigma \approx 36^\circ$, and an AGN bolometric luminosity of $L_{bol} \approx 2.6 \times 10^{43}$ erg s^{-1}.

Evidence of AGN activity at radio wavelengths is scarce: Stevens, Forbes & Norris (1999) consider evidence for a radio jet to be marginal at best, suggesting that star formation dominates the energetics at radio, optical, and soft X-ray wavelengths.

Being a nearby galaxy, isolated, with a prominent bar and spiral arms, and having an intermediate inclination with respect to the observer's line of sight, the gas kinematics in NGC 1365 have been extensively studied. This line of investigation was begun by Burbidge & Burbidge (1960) and Burbidge, Burbidge & Prendergast (1962) who used long slit spectroscopy to derive the rotation curve from Hα and [N II] observations. Significantly different kinematics were derived by Phillips et al. (1983) from observations of higher excitation lines, namely [O III] and He II. Jorsater & van Moorsel (1995) used high-resolution observations of neutral hydrogen to map the large-scale velocity field. They determined the inner disc ($120 \lesssim r \lesssim 240$ arcsec) inclination to be 40°. They also found non-circular motions associated with the bar, and a central reservoir of molecular gas. In the central region of the galaxy, a strongly disturbed velocity field was also revealed with the aid of optical observations by Lindblad et al. (1996a) while a biconical outflow model was proposed by Hjelm & Lindblad (1996) to explain the [O III] velocity field.

More recently, measurements of the large-scale 2D velocity field of Hα, and a new analysis of archival H I data, were presented in Zánmar Sánchez et al. (2008) who found strong asymmetries in the distribution of gas, dust and kinematical features, in both Hα and H I.

The galaxy NGC 1365 shares a number of similarities with NGC 1097, including morphology, distance, and inclination. It is not by chance that a number of authors have studied the two galaxies in parallel (e.g. Burbidge & Burbidge 1960; Ondrechen & van der Hulst 1989; Ondrechen, van der Hulst & Hummel 1989; Beck et al. 2005). In an earlier study of NGC 1097, Fathi et al. (2006), members of our team identified gas inflows along a nuclear spiral which leads down to a few parsecs from the unresolved AGN. It seems natural to look for similar inflows in NGC 1365. While previous spectroscopic studies have focused on the large-scale kinematics of NGC 1365, here we present optical integral field spectroscopy for the inner 6 arcsec. We adopt the distance of 18.6 ± 0.6 Mpc, as determined from Cepheid variables by Madore et al. (1999), which results in the scale $s = 90.2$ pc $arcsec^{-1}$.

The paper is organized as follows: observations and data reduction are described in Section 2, the data analysis, with details on the emission lines fitting procedures, is presented in Section 3. Results are given in Section 4 and discussed in Section 5. A summary of our findings is given in Section 6.

2 OBSERVATIONS AND DATA REDUCTION

NGC 1365 was observed on 2012 November 3 and 2013 January 18 with the Integral Field Unit (IFU) of the Gemini Multi-Object Spectrograph (GMOS; Allington-Smith et al. 2002; Hook et al. 2004) mounted on the Gemini South Telescope (program ID: GS-2012B-Q73). Two adjacent fields were observed, each covering 7 × 5 $arcsec^2$, resulting in a total angular coverage of 13 × 6 $arcsec^2$ with 0.2 arcsec sampling, centred on the nucleus, and roughly aligned with the nuclear bar. The observed field of view (FOV) is indicated

Downloaded from http://mnras.oxfordjournals.org/ at Universidade Federal do Rio Grande do Sul on October 26, 2016

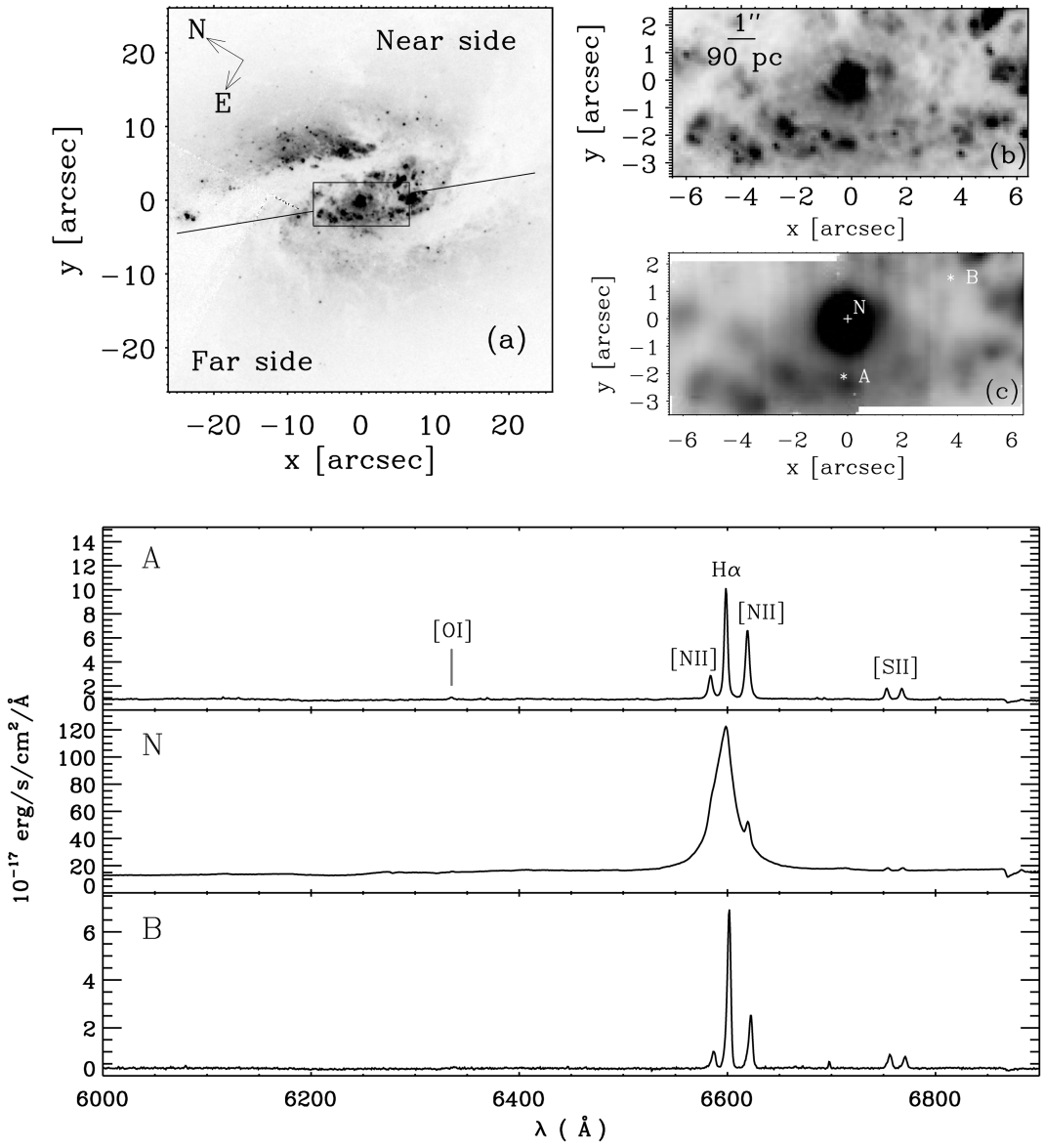

Figure 1. Top: (a) *HST* image of the nuclear region of NGC 1365 (WFPC2/WF - F547M, PID: 5222). The GEMINI field of view is shown as a box. The solid line indicates the line of nodes derived from the large-scale kinematics of neutral hydrogen (Jorsater & van Moorsel 1995). (b) Zoom-in on the *HST* image matching the GEMINI IFU field of view. (c) Continuum image extracted from the cube obtained with the GEMINI integral field unit. Bottom: representative spectra from the spaxels A, B and N, as indicated in the continuum image (c).

in the top left panel of Fig. 1; continuum images are shown in the right panels.

In order to account for dead fibres in the IFU, ±0.35 arcsec spatial dithering was applied along both axes. This resulted in four exposures of 2700 s each. From two images of the nuclear point source we determined that the spatial resolution is 0.58 ± 0.1 arcsec or 52 ± 9 pc, where the uncertainty represents a fiducial value for the variation of the seeing during the observation. The images of the nuclear point source were obtained by averaging the cube in the spectral direction within the range $6531 < \lambda < 6568$ Å, and $6632 < \lambda < 6656$ Å, that is the spectral region including, respectively, the blue and the red wing of the broad Hα emission.

In order to cover the wavelength range 5600–7000 Å, which includes the emission lines [O I]λ6300, Hα+[N II]λλ6548,6583, [S II]λλ6716,6731 and several stellar absorption features, we used the IFU in two-slits mode with the grating GMOS R400 in combination with the r(650 nm) filter, yielding a spectral resolution $R = 1918$. From the width of the emission lines in the spectrum of a calibration lamp, we estimate that the actual spectral resolution is $\sigma \approx 1.11$ Å, which corresponds to $\sigma \approx 49$ km s^{-1} within the range of wavelengths where the [N II]λ6583 emission line is observed. A portion of the spectrum including the most prominent emission lines is shown in the bottom panel of Fig. 1 for some representative positions in the FOV.

To perform data reduction we followed the procedure described in detail by Lena (2014). We used the IRAF[1] packages provided

[1] IRAF is the Image Reduction and Analysis Facility, a general purpose software system for the reduction and analysis of astronomical data. IRAF is written and supported by the National Optical Astronomy Observatories (NOAO) in Tucson, Arizona. NOAO is operated by the Association of

Downloaded from http://mnras.oxfordjournals.org/ at Universidade Federal do Rio Grande do Sul on October 26, 2016

by the GEMINI Observatory, and specifically developed for the GMOS instrument.[2] The process includes bias and sky subtraction, flat-fielding, trimming, wavelength and flux calibration, building of the data cubes, final alignment and combination of the four cubes. The final data cube has a spatial binning of 0.1 × 0.1 arcsec^2 and contains 7611 spectra. The fits to the strongest emission lines were performed with this binning. However, in order to fit the [O I] line, the signal-to-noise ratio was increased by re-binning to 0.2 × 0.2 arcsec^2, yielding 1920 spectra.[3] As the observations were carried out over a span of 10 weeks, heliocentric velocity corrections were applied to each cube before combination.

The typical accuracy in the wavelength calibration is 0.14 Å (or 6 km s^{-1} at $\lambda = 6583$ Å). Absolute flux calibration is uncertain because observations were obtained over a time span of three months, while only one observation of the standard star was performed. To verify the flux calibration, we compared the Hα flux derived here with the results of Schulz, Knake & Schmidt-Kaler (1994). In their table 3, they present the fluxes for both the narrow and broad Hα components, as derived with a spatial resolution of 3 arcsec, within an aperture of 2.6 × 6.5 arcsec^2, oriented along the east–west direction and approximately centred at 0.5 arcsec north of the nucleus. However, Schulz et al. stress that in their work there was 'no safely accurate positioning of the slit on the nucleus'. With this caveat, we note that they obtained 27 and 51 × 10^{-14} erg s^{-1} cm^{-2} for the fluxes of the narrow and the broad component, respectively. From the flux maps presented here, we obtain fluxes of 33 and 107 × 10^{-14} erg s^{-1} cm^{-2} for the two components. These quantities were measured within a box which reproduces, approximately, the settings adopted by Schulz et al.

The flux of the narrow component is in good agreement with the result of Schulz et al., while that derived for the broad component is larger by a factor of 2. The difference in the broad Hα flux is not too surprising since it can plausibly be attributed to intrinsic variability (AGN broad lines are well known to vary on time-scales of weeks to months; e.g. Peterson 1988); the difference in spatial resolution and the uncertain positioning of the slit in Schulz et al.'s observations may also contribute. The flux of the narrow component, on the other hand, should not show any strong variability over time, and it is not strongly affected by the slit position. Therefore, we consider the flux of the narrow component as the most reliable indicator of the flux calibration, and we conclude that the calibration adopted here compares well with the one used by Schulz et al.

3 EMISSION LINE FITTING

To model the continuum and the profiles of the most prominent emission lines (Hα, [N II]$\lambda\lambda$6548,6583, [S II]$\lambda\lambda$6716,6731, and [O I]λ6300), we used a customized version of the IDL[4] routine PROFIT (Riffel 2010). Either Gaussian or Gauss–Hermite profiles were fitted to the lines in order to derive centroid velocities, velocity dispersions and fluxes. Three separate runs were performed to fit the Hα + [N II] lines, the [S II] doublet, and the [O I] line. The continuum adjacent to the lines was modelled with a first-order polynomial.

Universities for Research in Astronomy (AURA), Inc. under cooperative agreement with the National Science Foundation.

[2] http://www.gemini.edu/sciops/data-and-results/processing-software?q=node/11822

[3] Of the maps presented in this paper, only the [O I]/Hα map (Fig. 7) was derived from the cube binned to 0.2 × 0.2 arcsec^2.

[4] IDL, or Interactive Data Language, is a programming language used for data analysis and visualization.

Table 1. The broad components.

Component	Vel (km s^{-1})	σ (km s^{-1})	Relative flux (amplitude)
1	−143 ± 1	394 ± 1	1 (1)
2	−51 ± 2	1113 ± 2	0.893 (0.411)
Tot	−100 ± 2*	1181 ± 2†	...

Notes. *This is a flux-weighted average of the velocities derived for the two components. All velocities have been computed after subtracting a systemic velocity of 1671 km s^{-1}.

†This value is computed as $\sqrt{\sigma_1^2 + \sigma_2^2}$. Fluxes are free parameters with a different value for each pixel. As a reference, for both Gaussians the median flux per pixel within a radius of 0.3 arcsec from the continuum peak is 1.2 × 10^{-14} erg s^{-1} cm^2, where 1 pixel ≡ 0.1 × 0.1 arcsec^2.

Despite the presence of several bright star-forming regions, it is difficult to derive information on the stellar kinematics: over the region where the AGN point-spread-function (PSF) dominates, the AGN continuum is much stronger than the underlying stellar component. Moreover, within the covered spectral range, the only prominent absorption lines due to a young stellar population are the Na I doublet, and Hα. The first one is contaminated by neutral gas; the second one is hidden under the strong Hα emission due to the ionized gas. Because of this, the fit of a stellar template would be poorly constrained and we chose not to do it. In principle, the Hα flux should be corrected for the underlying stellar absorption, but, because the Hα emission line is very strong, we estimate that this correction is smaller than the error in the line flux (Section 4.2.1).

3.1 Fitting procedure

To fit the Hα + [N II] emission lines we assumed that (i) the narrow component of Hα and [N II]λ6548 has the same width as [N II]λ6583; (ii) the [N II]λ6548 emission line has the same redshift as [N II]λ6583; (iii) the amplitude of [N II]λ6548 is 1/2.96 times the [N II]λ6583 amplitude (e.g. Osterbrock & Ferland 2006). A similar approach was used to fit the [S II] doublet: we assumed that both lines have the same redshift and width; however the amplitude of each line was left as a free parameter.

Over most of the FOV, the emission lines are well represented by a simple Gaussian profile, e.g. top left panel in Fig. 2, however a bright broad Hα line is present at the nucleus, e.g. spectrum N in the bottom panel of Fig. 1, and the emission lines exhibit asymmetric bases over certain regions of the FOV, e.g. spectrum B in the bottom panel of Fig. 1. The strategies adopted to fit the emission line profiles are described below for each case.

The broad line region (BLR): the central 0.6 arcsec is dominated by unresolved emission from the BLR which manifests itself in the form of a broad Hα emission line. At the nucleus it dominates the underlying narrow component and is still visible as a broad base up to 2 arcsec from the nucleus, tracing the extended wings of the PSF.

As the BLR is unresolved, we fitted it with a combination of two Gaussians for which only the total flux was left as a free parameter. We used three spaxels located at different positions around the nucleus at a radius of approximately 0.5 arcsec to determine the width, velocity and relative flux of the two Gaussians. In these spaxels the narrow emission lines associated with [N II] and Hα are strong enough with respect to the broad component to robustly constrain the fit to the line profile. The mean values of the parameters derived from these fits are shown in Table 1. A fit performed at the nucleus using these parameters is shown in the top right panel of Fig. 2. The underlying narrow emission lines corresponding to [N II] and Hα were fitted simultaneously.

Downloaded from http://mnras.oxfordjournals.org/ at Universidade Federal do Rio Grande do Sul on October 26, 2016

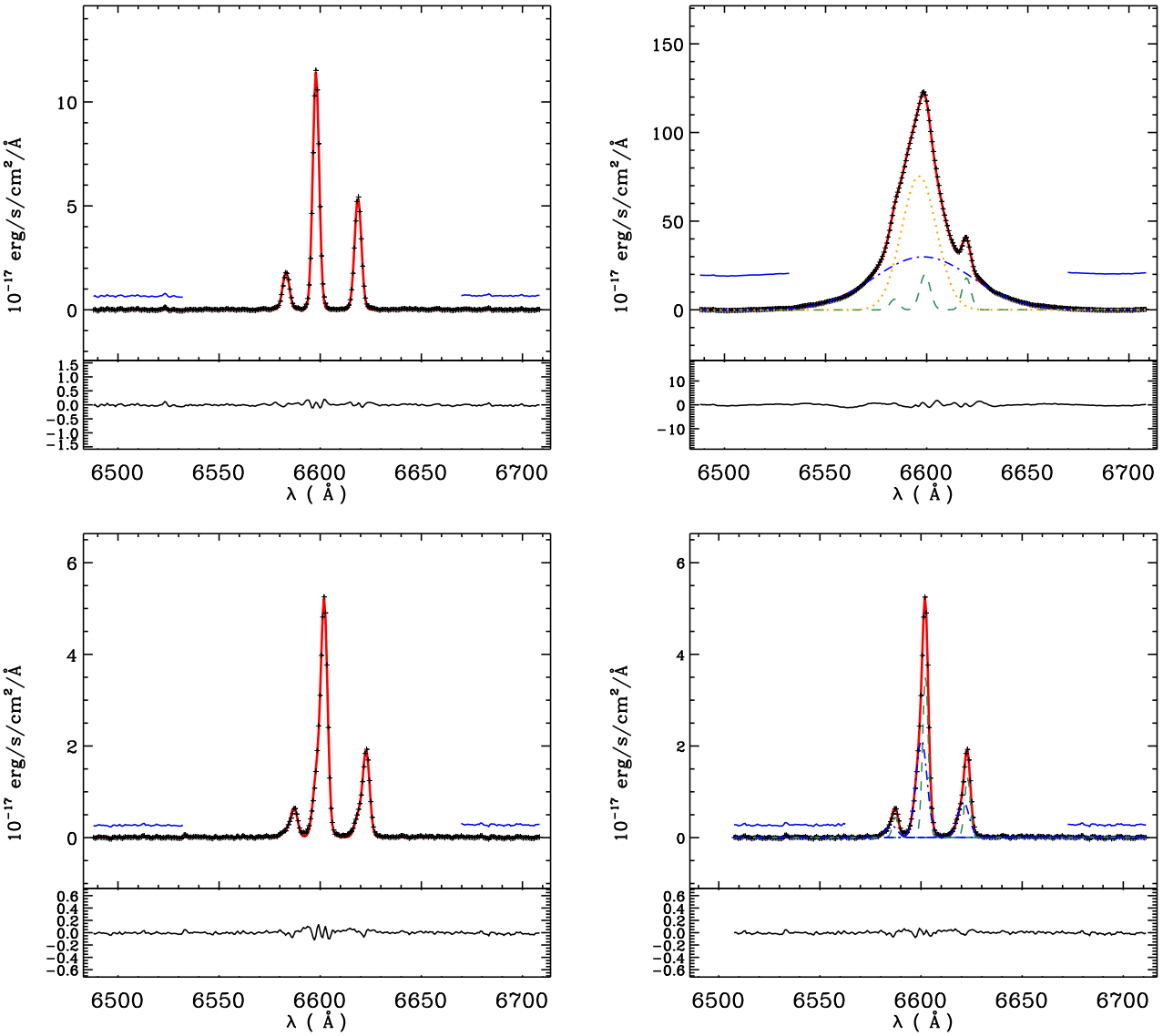

Figure 2. Fit of the [N II]λλ6548,6583 and Hα emission lines. Top left: example of single Gaussian fit. The horizontal blue lines mark the continuum level before it was subtracted. Top right: fit at the nucleus. Two Gaussians were used to model the broad Hα (blue dot–dashed and orange short-dashed). The green long-dashed Gaussians represent the underlying narrow components. Bottom left: example of a fit with Gauss–Hermite polynomials. Bottom right: same spectrum shown in the previous panel, but in this case modelled with two Gaussians to extract the velocity of the component associated with the asymmetry (blue dot–dashed Gaussian).

Asymmetries (Gauss–Hermite polynomial fit): asymmetric line profiles are present in some regions of the FOV. To map the spatial distribution of the asymmetry we fitted the emission lines with a truncated Gauss-Hermite polynomial (GHP):

$$f_{gh}(\lambda) = F\frac{e^{-k^2/2}}{\sqrt{2\sigma^2}}(1 + h_3H_3 + h_4H_4) \quad (1)$$

$$H_3 = \frac{1}{\sqrt{\sigma}}\left(2\sqrt{2}k^3 - 3\sqrt{2}k\right) \quad (2)$$

$$H_4 = \frac{1}{\sqrt{24}}\left(4k^4 - 12k^2 + 3\right) \quad (3)$$

$$k = \frac{(\lambda - \bar{\lambda})}{\sigma}, \quad (4)$$

where F is the flux, σ the velocity dispersion, and $\bar{\lambda}$ the peak wavelength. Departures from symmetry are quantified by the value of the coefficient h_3, a proxy for the skewness: a negative (positive) value of this coefficient indicates the presence of a blueshifted (redshifted) tail. The coefficient h_4, a proxy for the kurtosis, measures the degree of 'peakiness' of the emission line: a negative (positive) value of this coefficient indicates a boxy (centrally peaked) line profile. An example of a spectrum fitted with a GHP is shown in the bottom left panel of Fig. 2.

It is reasonable to argue that asymmetries in the line profile originate from a superposition of multiple kinematical components (e.g. gas rotating in a disc plus gas experiencing in/outflow). While the GHP allows us to derive accurate fluxes for the total line profile, it does not disentangle the multiple components. To achieve this goal, we also fit the asymmetric line profiles with two Gaussians.

Downloaded from http://mnras.oxfordjournals.org/ at Universidade Federal do Rio Grande do Sul on October 26, 2016

Asymmetries (two Gaussians fit): to derive flux, velocity dispersion and velocity for the kinematical component responsible for the observed asymmetry, we fitted two Gaussians to those lines where the skewness coefficient satisfies the condition $|h_3| \geq 0.05$. The condition was determined by trial and error to select those regions where the asymmetry is strong enough to allow a robust fit with two Gaussians. An example of a two-component fit is shown in the bottom right panel of Fig. 2.

3.2 Uncertainties

To estimate the errors on the measured quantities we performed Monte Carlo simulations: for each spaxel, we constructed 100 realizations of the spectrum by adding Gaussian noise with amplitude comparable to the noise measured in the original spectrum. Mean values and standard deviations for the centroid velocities, velocity dispersions and fluxes were derived for each spaxel, with the standard deviation of the distribution in each parameter being taken as the uncertainty.

4 RESULTS

4.1 Velocity and velocity dispersion

The centroid velocity and velocity dispersion derived from the narrow [N II]λ6583 emission line are shown in Fig. 3. The maps were produced by combining results from the single-Gaussian fit and the multiple component fit to the spectra where a broad Hα line is present.

The intrinsic velocity dispersion was derived as:

$$\sigma_{\rm int} = \sqrt{\sigma^2_{\rm obs} - \sigma^2_{\rm ins}}, \quad (5)$$

where $\sigma_{\rm obs}$ is the observed velocity dispersion, as derived from the fit of the emission lines, and $\sigma_{\rm ins}$ is the instrumental broadening, as derived from the fit of the emission lines in the spectra of a calibration lamp. Within the range of wavelengths where the [N II]λ6583 emission line is observed, that is $6610 < \lambda < 6630$ Å, $\sigma_{\rm ins}$ can be approximated to 49 km s^{-1}. After the correction is applied, the velocity dispersion ranges between 35 and 105 km s^{-1} with a mean value of 62 km s^{-1} (approximately coincident with the median).

The velocity field shows a pattern which could originate either from rotation or streaming motions along a bar. Hints that an additional kinematical component is superposed on the velocity field derived from the narrow component come from asymmetries in the base of the line profiles. A map of the skewness of the emission lines, the h_3 coefficient derived from Gauss–Hermite polynomial fits, is presented in the top panel of Fig. 4. A comparison of this map with the velocity field in Fig. 3 makes it clear that the asymmetry is reversed with respect to the velocity field of the narrow component, i.e. the asymmetry is blueshifted (redshifted) where the emission lines are redshifted (blueshifted) with respect to the systemic velocity. In regions where $|h_3| \geq 0.05$ each line was modelled with two Gaussians. The centroid velocity and velocity dispersion for the component associated with the asymmetry are presented in Fig. 5.

The BLR is assumed to be unresolved, therefore the kinematical parameters used to fit the broad Hα components were not allowed to vary over the FOV. Values for the velocity and velocity dispersion adopted for each Gaussian component are listed in Table 1.

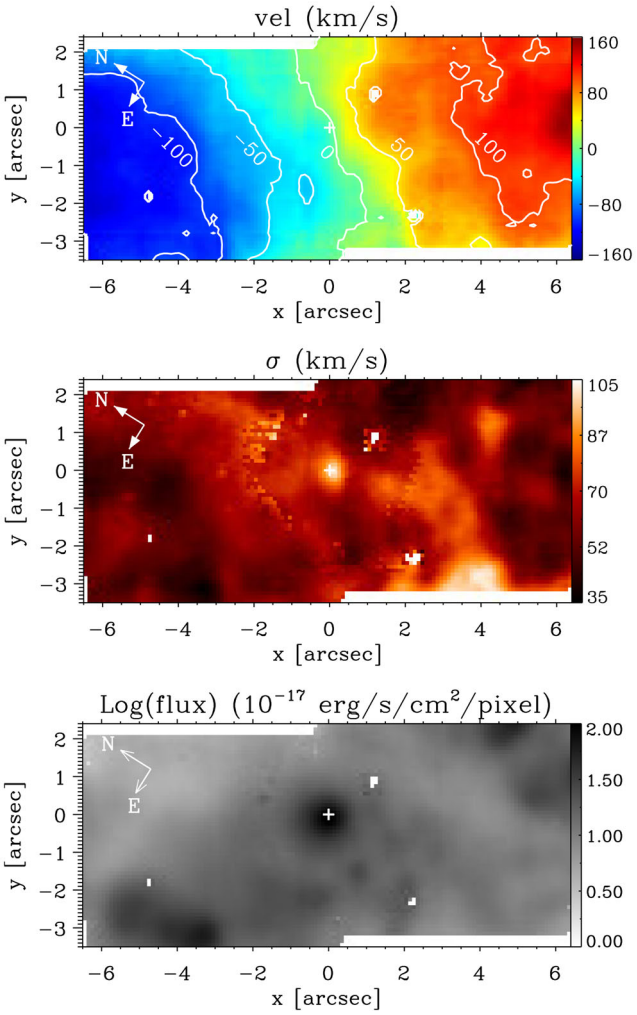

Figure 3. Maps derived by fitting a Gaussian profile to the narrow component of the [N II] emission line. Top: velocity. Centre: velocity dispersion. Bottom: flux. The velocity map is shown after subtracting a systemic velocity of 1671 km s^{-1} (derived from the modelling described in Section 5.1). The cross at (0,0) marks the continuum brightness peak.

Centroid velocities and velocity dispersions derived from the fits to the Hα, [S II], and [O I] emission lines are consistent with the values derived from [N II].

4.1.1 *Uncertainties*

Errors due to the fitting procedure, on the velocity and velocity dispersion, were estimated with a Monte Carlo simulation, as explained in Section 3.2. The uncertainty values derived for the single Gaussian fit are typically lower than 1 km s^{-1} for the centroid velocity of the [N II] and Hα narrow lines. Errors are slightly larger for the [S II] lines, but still below 5 km s^{-1}, with a median value approximately equal to 1 km s^{-1}. Typical errors of 5 km s^{-1} are associated with the velocity derived from the [O I] line. Similar values were obtained for the velocity dispersion.

Typical errors for the asymmetric component are approximately 1 km s^{-1} for both the velocity and velocity dispersion in the right side of the FOV, where the asymmetry is stronger. In the left side, where the asymmetry is weaker, typical errors are approximately 10 km s^{-1}.

Downloaded from http://mnras.oxfordjournals.org/ at Universidade Federal do Rio Grande do Sul on October 26, 2016

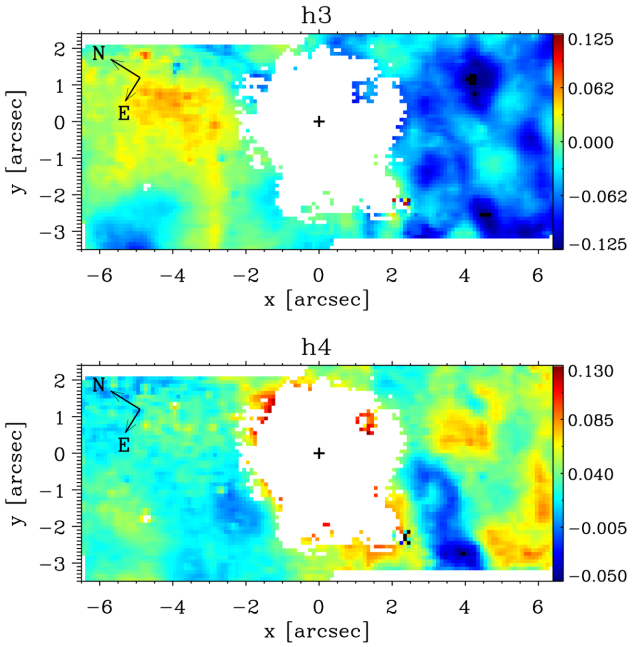

Figure 4. Maps of the Gauss–Hermite coefficients h_3 and h_4. The central region was excluded because of the presence of a broad Hα component which did not allow a reliable fit with Gauss–Hermite polynomials. As a reference, a spectrum extracted from the region close to (4.5 arcsec, 1 arcsec), where the asymmetry reaches the maximum, is presented in the bottom panel of Fig. 2.

Errors for the velocity and velocity dispersion of the broad Gaussians used to model the broad Hα are given in Table 1.

4.2 Line fluxes

The flux maps for the [N II], Hα, [S II], and [O I] emission lines all show roughly the same general structures, although there are differences in detail. For example, the integrated flux distribution for the [N II]λ6583 emission line is shown in the bottom panel of Fig. 3: the strongest emission is observed at the nucleus; two bright blobs, probably H II regions, are visible approximately 5 arcsec north-east and south-west of the nucleus. There are also several fainter blobs, like those in a ring-like structure around the nucleus, at a distance of 1–2 arcsec. As the main features are similar, the flux maps for Hα, [S II], and [O I] are not shown, but these were used to construct the line ratio maps, [N II]/Hα, [S II]/Hα and [O I]/Hα, which are presented in Fig. 7 and discussed in Section 4.4.

The flux map for the asymmetric component fitted to [N II] and Hα is shown in the bottom panel of Fig. 5.

4.2.1 Uncertainties

Uncertainties on the fluxes, as derived from the fitting procedure, have been estimated with the Monte Carlo simulation described in Section 3.2. Typical uncertainties are below 10 per cent on both fluxes and flux ratios for the strongest lines, i.e. [N II] and Hα. Typical uncertainties on the fluxes of the weaker lines are approximately 10 per cent, corresponding to an uncertainty of about 15 per cent on the flux ratio.

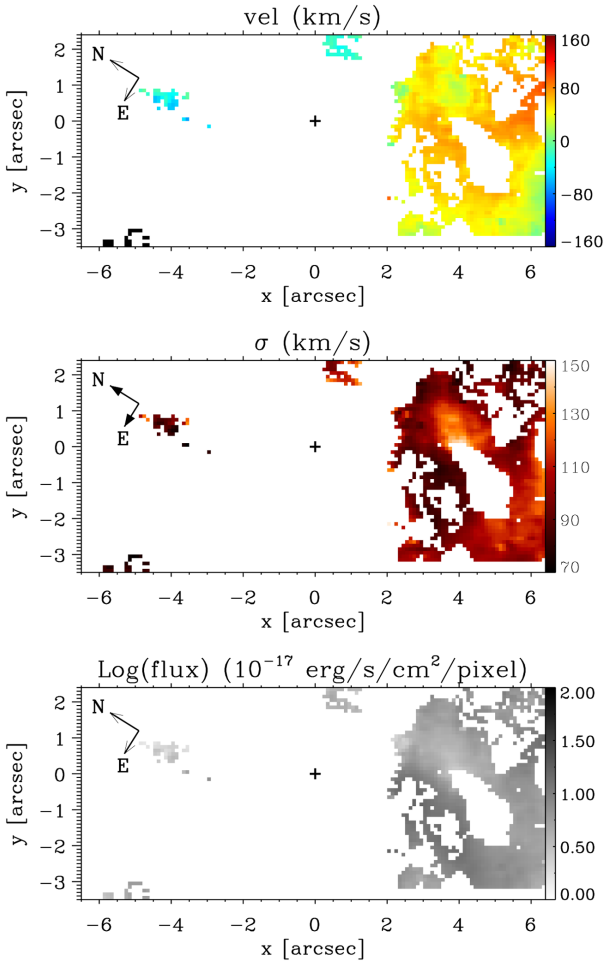

Figure 5. Maps derived by fitting two Gaussians to the [N II]λ6583 emission lines characterized by a skewness $|h_3| \geq 0.05$. Maps shown here represent the asymmetric component. Top: velocity. Centre: velocity dispersion. Bottom: flux. The velocity map is shown after subtracting a systemic velocity of 1671 km s^{-1}.

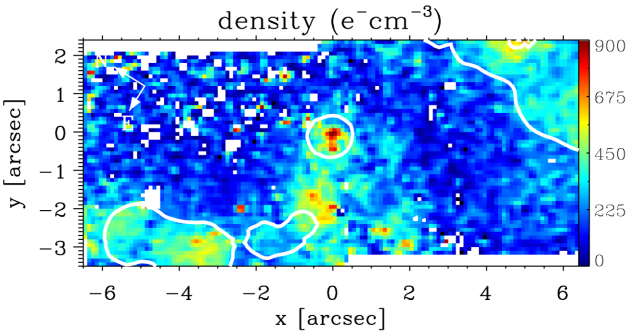

Figure 6. Electron density map derived from the flux ratio [S II]$\lambda\lambda$6716/6731 assuming a temperature $T = 10^4$ K. The solid white contours mark the most prominent features visible in the Hα flux map.

4.3 Electron density

The electron density is shown in Fig. 6. It was derived from the intensity ratio [S II]λ6716/λ6731 assuming a temperature of 10^4 K (Osterbrock & Ferland 2006).

Downloaded from http://mnras.oxfordjournals.org/ at Universidade Federal do Rio Grande do Sul on October 26, 2016

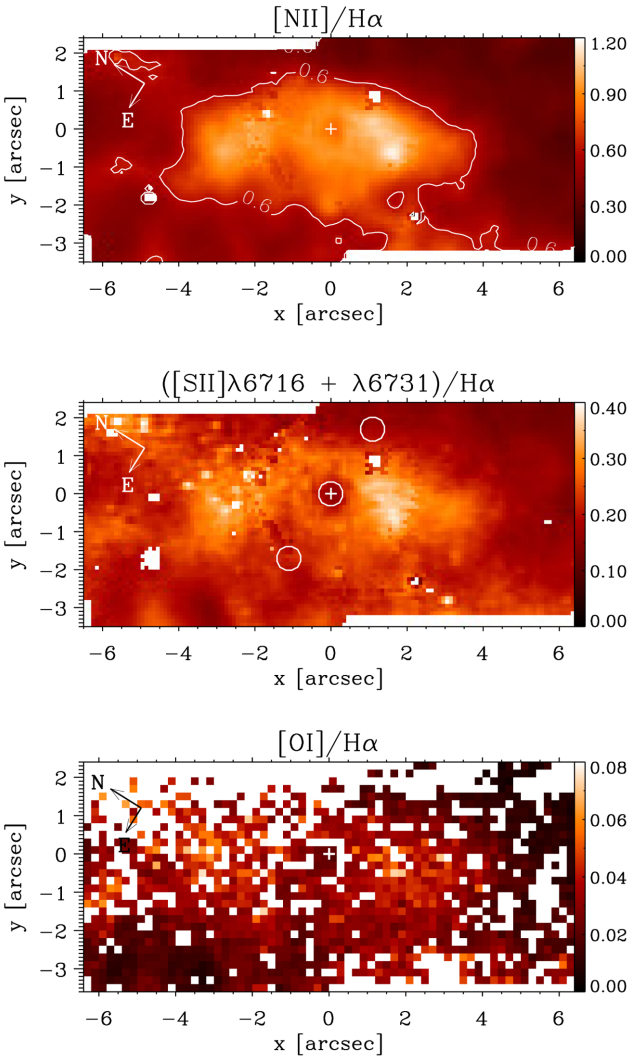

Figure 7. Flux ratios [N II]λ6583/Hα, [S II](λ6716 + λ6731)/Hα and [O I]λ6300/Hα. Spaxels where the relative error on the ratio is equal to or larger than 50 per cent have been masked out (blank pixels). A contour corresponding to [N II]/Hα = 0.6 is plotted in the top panel; [N II]/Hα > 0.6 (log 0.6 = −0.2) is characteristic of AGN photoionization. Solid circles in the central panel highlight the regions used to extract the data plotted in the BPT diagrams.

The map shows values in the range 100–200 cm^{-3} over most of the FOV, with a typical uncertainty of 60 cm^{-3}. The density increases to a mean value of 600 ± 100 cm^{-3} within a radius of ≈0.5 arcsec from the nucleus. High values (≈500 ± 100 cm^{-3}) are present east and south-east of the nucleus, in a region coincident with the cone of [O III]λ5007 emission reported by Storchi-Bergmann & Bonatto (1991). Similar high densities are present in the bright blobs, already identified in the flux maps, located about 5 arcsec north-east and south-west of nucleus.

It was not possible to perform a robust fit of the [S II] doublet with two Gaussians, therefore a density map for the asymmetric component was not derived.

4.4 Line ratios

Maps for the line ratios [N II]λ6583/Hα, [S II](λ6716 + λ6731)/Hα and [O I]λ6300/Hα are presented in Fig. 7. Spaxels where relative errors are equal or larger than 50 per cent have been masked out.

The maps show high values in an elongated region, roughly centred on the nucleus, extending from −4 to +4 arcsec along the NE–SW direction, and approximately 1.5 arcsec NW and SE of the nucleus, in the orthogonal direction. In this region typical values range between 0.8 (log: −0.1) and 1.2 (log: 0.08) for [N II]/Hα, between 0.25 (log: −0.6) and 0.36 (log: −0.4) for [S II]/Hα, and between 0.03 (log: −1.5) and 0.05 (log: −1.3) for [O I]/Hα. A decrease in the line ratios is visible in the maps within 0.5 arcsec from the nucleus, but it is more pronounced in the [S II]/Hα ratio, whose values drop into the range 0.15–0.24 (log: −0.8, −0.6). Low values are also visible in a large region approximately west of the nucleus. Values are in the range 0.26–0.4 (log: −0.6, −0.4) for the [N II]/Hα ratio, 0.12–0.17 (log: −0.9, −0.8) for the [S II]/Hα ratio, and 0.007–0.01 (log: −2.15, −2) for the [O I]/Hα ratio. Intermediate values are present north, east and south of the nucleus.

The increase in the line ratios, in the NE–SW direction, is fairly well defined and evident. It does not have any clear corresponding feature in the density or in the kinematical maps; however it is confined within the elongated ring of bright knots clearly visible in the *Hubble Space Telescope* (*HST*) continuum images (compare the top panel of Fig. 7 with the top right panel in Fig. 1). It is possible that the increase in the line ratio traces the region where AGN photoionization dominates over stellar photoionization.

The decrease in the line ratios at the nucleus is larger than the associated uncertainty, especially for the [S II]/Hα ratio. However, given the complexity of the spectral profiles we may wonder whether the decrease is reliable or due to misfits of the spectral lines. The modelling of the Hα and [N II] doublet, at the nucleus, is not well constrained because of heavy line blending. Although visual inspection of the fits suggests that this assumption produces a satisfactory fit of the lines, it is possible that the amplitude of the narrow Hα is slightly overestimated, producing a decrease in the [N II]/Hα ratio. Another possibility is that the decrease in the line ratios is due to an increase of the ionization parameter[5] in the immediate vicinity of the AGN (e.g. Ferland & Netzer 1983). The decrease of the [N II]/Hα ratio at the nucleus might be less pronounced than is the case for the other line ratios because [N II]/Hα is more sensitive to AGN photoionization, which causes [N II]/Hα to increase (Kewley et al. 2006).

Schulz et al. (1999) provide values for the [O III]/Hβ ratio at three locations within our FOV: at the nucleus, 2 arcsec east and 2 arcsec west of the nucleus. We derived [N II]/Hα, [S II]/Hα and [O I]/Hα line ratios at those locations within an extraction aperture of radius 0.3 arcsec (see the middle panel in Fig. 7). The corresponding values are plotted in the BPT diagrams (Baldwin, Phillips & Terlevich 1981) presented in Fig. 8.

Bearing in mind that [O III] and Hβ line fluxes were not obtained simultaneously with the remaining line fluxes, nor at the same spatial resolution, it is worth noting that one point ('west') falls in the H II region of all three diagrams, whereas the other two ('nucleus' and 'east') fall close to the boundary with the AGN region. This suggests that AGN and stellar photoionization mechanisms coexist with similar energetics even at the very nucleus of the galaxy.

[5] That is the ratio between the density of ionizing photons and the density of the gas (e.g. Osterbrock & Ferland 2006).

Downloaded from http://mnras.oxfordjournals.org/ at Universidade Federal do Rio Grande do Sul on October 26, 2016

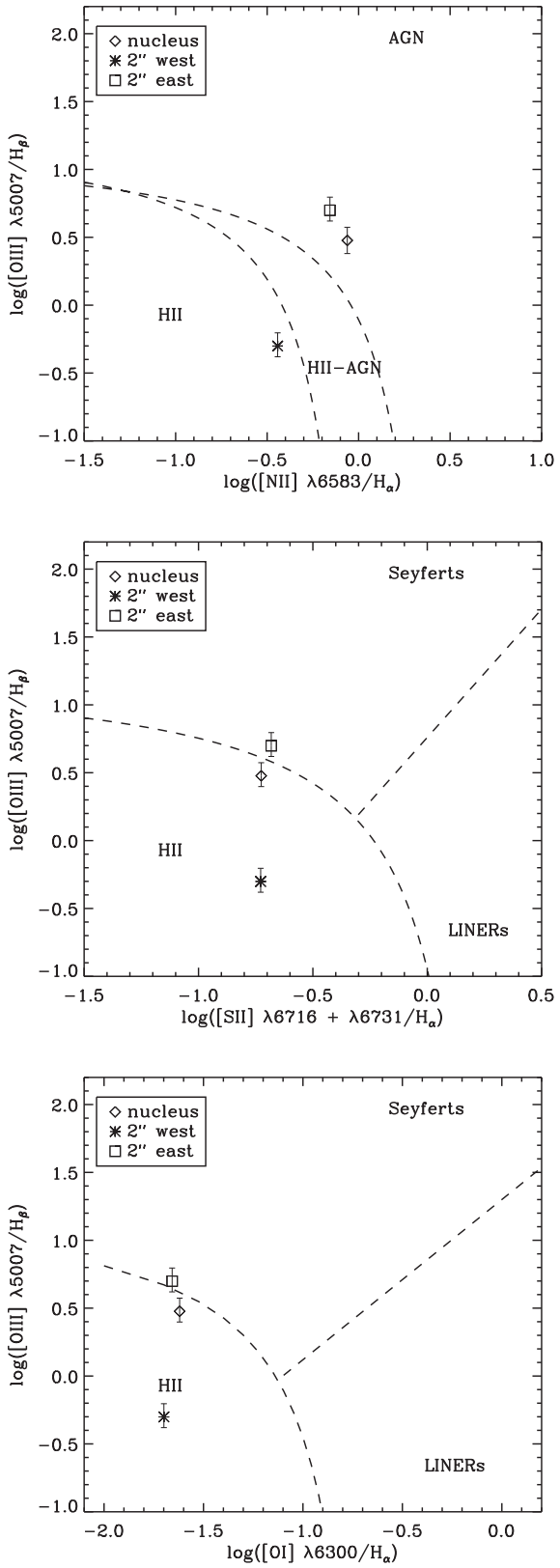

Figure 8. BPT diagrams for line ratios computed over circular regions of 0.3 arcsec in radius centred at the nucleus, and 2 arcsec east and west of the nucleus as indicated in the middle panel of Fig. 7. Values for the [O III]/Hβ ratio have been taken from Schulz et al. (1999). Horizontal error bars are approximately of the same size of the symbols. The dashed boundary lines are taken from Kewley et al. (2006).

Table 2. Fits to the observed gaseous velocity field.

Parameter		Notes	Initial guess
A (km s^{-1}).....	218	...	100:400
v_{sys} (km s^{-1})....	1671 ± 6*	Heliocentric	800:2400
ψ_0 (deg).....	15†	...	10:60
c_0 (arcsec).....	3.6	...	0:10
p.....	1	Fixed	...
θ (deg).....	41	Fixed	...
x_0 (arcsec).....	0	...	−2:2
y_0 (arcsec).....	−0.5	...	−2:2

Notes. *The systemic velocity derived from the narrow lines at the continuum peak is 1659 ± 6 km s^{-1}.
†This value corresponds to a position angle on the sky of 250° east of north.

5 DISCUSSION

5.1 Non-circular motions in the gas velocity field

With the goal of isolating non-circular motions, we fitted the [N II] velocity field with a kinematic model describing circular orbits in a plane (van der Kruit & Allen 1978; Bertola et al. 1991):

$$v_{\rm mod}(r,\psi) = v_{\rm sys} + \frac{Ar\cos(\psi-\psi_0)\sin\theta\cos^p\theta}{\{r^2[\sin^2(\psi-\psi_0)+\cos^2\theta\cos^2(\psi-\psi_0)]+c_0^2\cos^2\theta\}^{p/2}}. \quad (6)$$

This yields a velocity curve that increases linearly at small radii and becomes proportional to $r^{(1-p)}$ at large radii. The parameter $v_{\rm sys}$ is the systemic velocity, A is the amplitude of the rotation curve, r and ψ are the radial and angular coordinates of a given pixel in the plane of the sky, ψ_0 is the position angle of the line of nodes measured with respect to the image x-axis (increasing counter-clockwise). The disc inclination is θ ($\theta = 0$ for face-on discs). The parameter p measures the slope of the rotation curve where it flattens, in the outer region of the galaxy, varying in the range 1–1.5. Finally, c_0 is a concentration parameter which gives the radius at which the velocity reaches 70 per cent of the amplitude A.

As shown in Zánmar Sánchez et al. (2008) and other previous studies, the velocity curve of NGC 1365 is still rising within the region probed by our observations, therefore the parameters p, A (and therefore c_0) are poorly constrained by the data. We assume $p = 1$, which corresponds to an asymptotically flat rotation curve at large radii. We keep A and c_0 as free parameters; however these should not be taken as characteristic of the large-scale rotation curve of the galaxy. The model fitted here has the sole purpose of isolating non-circular motions.

The inclination θ has been estimated in previous works from both photometry ($\theta = 51°$, e.g. Lindblad 1978; Zánmar Sánchez et al. 2008) and the large-scale kinematics ($\theta = 41°$, e.g. Jorsater & van Moorsel 1995; Zánmar Sánchez et al. 2008). We adopted the latter value, $\theta = 41°$, holding it fixed in the fit. Both Jorsater & van Moorsel and Zánmar Sánchez et al. show that the photometric value produces a poor fit to the kinematics, suggesting that the discrepancy is likely due to the strong spiral features located close to the major axis (e.g. Barnes & Sellwood 2003).

To determine the parameters (A, $v_{\rm sys}$, ψ_0, c_0) and the centre of the rotation field (x_0, y_0), we fitted the rotation model defined by equation (6) to the [N II] velocity map. The fit was performed with a customized IDL routine which makes use of the fitting engine MPFIT (Markwardt 2009) to implement a Levenberg–Marquardt least-squares algorithm. The derived parameters are listed in Table 2. Maps of the observed and the best-fitting model velocity field are shown in Fig. 9 together with the residual map.

Downloaded from http://mnras.oxfordjournals.org/ at Universidade Federal do Rio Grande do Sul on October 26, 2016

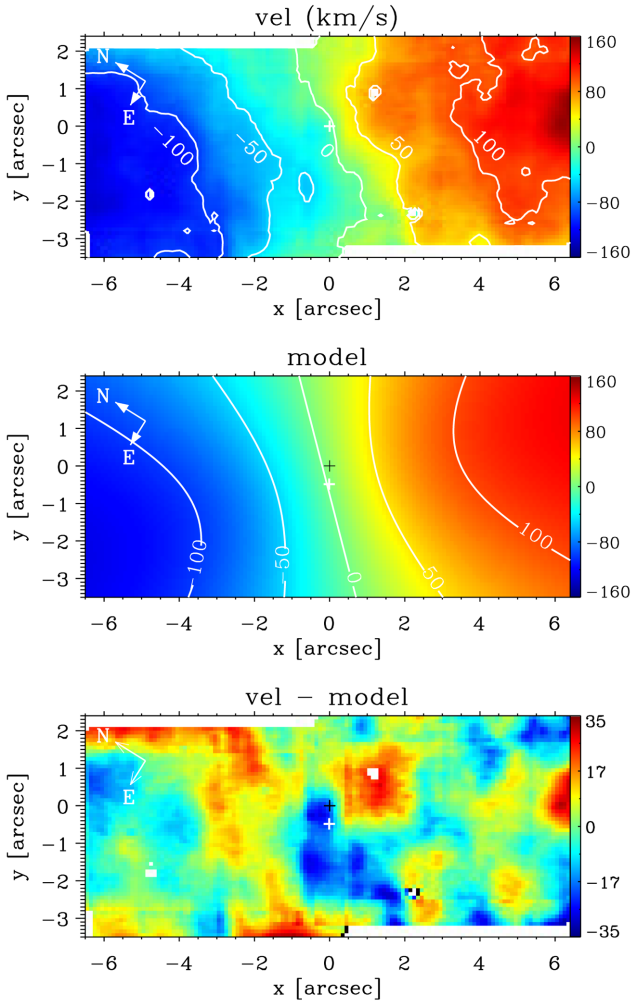

Figure 9. Maps derived from the fit to the narrow component of the [N II] emission line. Top: observed velocity field. Centre: model. Bottom: residual. The velocity map is shown after subtracting a systemic velocity of 1671 km s^{-1}, derived from the fit. The black cross at (0,0) marks the continuum brightness peak. The white cross marks the kinematical centre derived from the fit.

The position angle of the line of nodes that we derived from the fit (250° east of north) is substantially different from the value derived from the large-scale kinematics (220°; Jorsater & van Moorsel 1995; Zánmar Sánchez et al. 2008). This is not surprising because the galaxy is strongly barred and we probed a much smaller region than that studied by Jorsater & van Moorsel and Zánmar Sánchez et al. However, a visual comparison between the [N II] velocity map derived here and the large-scale Hα velocity map presented in fig.4 of Zánmar Sánchez et al. shows that we obtain consistent results for the gas kinematics in the inner 6 arcsec.

The systemic velocity that we obtained from the fit of the kinematical model is 1671 ± 6 km s^{-1} (heliocentric). This value is significantly different from the value derived from the large-scale gas kinematics (1632 km s^{-1}; Jorsater & van Moorsel 1995; Zánmar Sánchez et al. 2008). However, it is consistent with the average systemic velocity derived from the optical measurements listed on the Hyperleda extragalactic data base,[6] that is 1657 ± 10 km s^{-1}.

[6] http://leda.univ-lyon1.fr/

We found that the kinematical centre is offset 0.5 arcsec southeast of the continuum peak (comparable with the PSF FWHM, which is approximately 0.6 arcsec). From the large-scale gas kinematics Zánmar Sánchez et al. found an offset of a few arcsec.

The velocity residuals have an amplitude distribution that is well represented by a Gaussian approximately centred at 1 km s^{-1} with an FWHM of 27 km s^{-1}. Interpretation of the residual spatial distribution is not straightforward: the bottom panel in Fig. 9 shows that a number of deviations from circular motion are present over the field. Most of such deviations take the form of blobs with a typical size of about 1 arcsec and an amplitude in the range 10–20 km s^{-1}. There is no clear correspondence between the residuals and the spatial flux distribution of the Hα emission line. In particular, the bright knots NE and SW of the nucleus do not correspond to features in the velocity residual map. Therefore, the residuals do not appear to be associated with the circum-nuclear star-forming regions.

The most interesting feature is a negative residual extending south-eastward from the continuum peak down to the edge of the FOV. This extended blueshifted residual derived from the [N II] velocity field is located within the well-known [O III] ionization cone (e.g. Storchi-Bergmann & Bonatto 1991; Sharp & Bland-Hawthorn 2010).

5.1.1 *Uncertainties*

Uncertainties due to the noise on the parameters presented in Table 2 are negligible.

We tested the dependence of the recovered parameters on the initial guess and found that, using initial values drawn randomly from the range specified in Table 2, the solution was stable converging, almost always, to the same values. In only a few cases (5/200) did the algorithm recover a solution which was clearly not acceptable. It seems, therefore, that the solution is robust against a fairly large range of initial guesses.

The main source of uncertainty seems to be the wavelength calibration. As already stated in Section 2, the random error was estimated to be 6 km s^{-1}. However, the calibration can be affected by systematics which are difficult to assess because of the lack of suitable sky lines within the observed spectral range. To understand how a systematic error on the wavelength calibration would affect our results, we repeated the modelling of the velocity map after adding (subtracting) a constant value of 40 km/s (which is the difference between the systemic velocity measured here and the value derived by Jorsater & van Moorsel 1995 and Zánmar Sánchez et al. 2008). We found that the pattern and amplitude of the velocity residuals are virtually unchanged. Apart from the systemic velocity, for which we measure differences of 40 km/s, as expected, none of the other parameters shows any significant variation.

5.2 Evidence for an outflow?

Since the early observations of NGC 1365 (e.g. Burbidge & Burbidge 1960; Burbidge et al. 1962) it has been clear that the circum-nuclear gas kinematics is complex and that outflows could be present. Two decades later, Phillips et al. (1983) observed split [O III] lines a few arcsec from the nucleus and, inspired by the work that Axon & Taylor (1978) had recently published on M82, they proposed a model where the [O III] emission originated from material outflowing along the walls of a hollow cone. A one-sided fan-shaped morphology was observed in [O III] by, e.g. Edmunds et al. (1988) and Storchi-Bergmann & Bonatto (1991), while later

Downloaded from http://mnras.oxfordjournals.org/ at Universidade Federal do Rio Grande do Sul on October 26, 2016

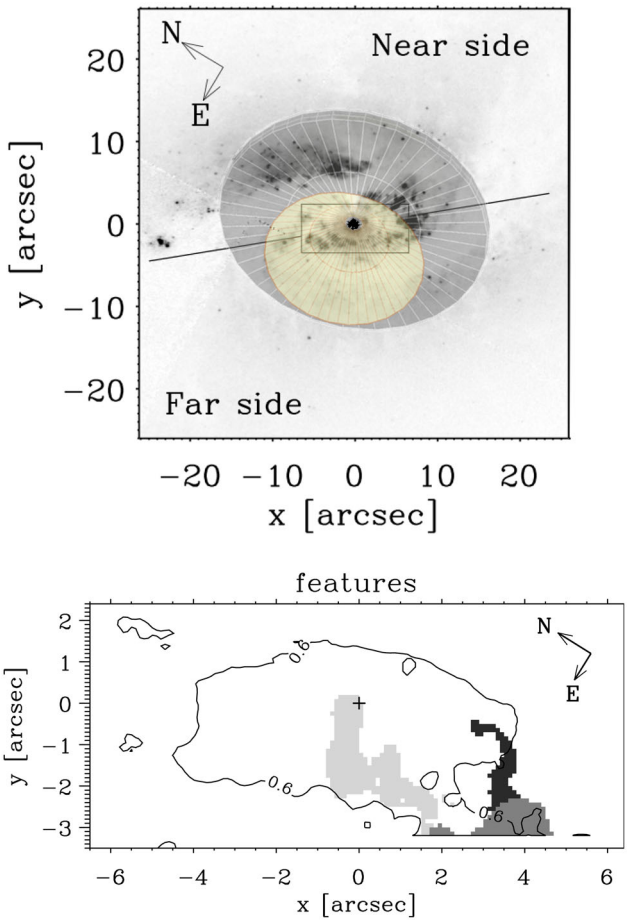

Figure 10. Top: as in Fig. 1, with a cartoon representing the plane of the galaxy (large grey disc) and the approaching AGN radiation cone (in yellow, cartoon made with the SHAPE software; Steffen et al. 2011). Bottom: map of the observed features suggestive of outflowing gas: fan-shaped blueshifted velocity excess coincident with enhanced electron density (light grey), clear evidence for a second spectral component, suggestive of unresolved split lines (dark grey), flat-topped line profiles suggestive of unresolved split lines (black and dark grey). The solid line corresponds to [N II]/Hα = 0.6, as in Fig. 7. Points inside the contour are characterized by [N II]/H$\alpha \geq 0.6$, suggestive of AGN photoionization.

observations provided evidence for a counter fan (Veilleux et al. 2003; Sharp & Bland-Hawthorn 2010).

A number of observations were performed to confirm and understand the line splitting, and a number of models were proposed (e.g. Jorsater, Lindblad & Boksenberg 1984; Edmunds et al. 1988; Hjelm & Lindblad 1996). The current consensus is that the velocity field derived from low-ionization lines (e.g. Hα and [N II]λ6585) is consistent with rotation in a disc, while the velocity field derived from [O III] traces a biconical outflow. According to the model proposed in Hjelm & Lindblad (1996), the line splitting is due to the superposition of two spectral components: one originating from gas rotating in the galaxy disc, and one outflowing in a cone. The cone has a half opening angle of 50°, the axis is within 5° of the galaxy rotation axis, and the outflow is radially accelerated with higher velocities close to the cone axis. See the top panel in Fig. 10, or Hjelm & Lindblad (1996) and Lindblad (1999), for illustrations of the geometry described above.

Evidence for an outflow coincident with the extended [O III] emission is not obvious in the velocity field derived from the [N II] emission. However, as described in the previous section, the velocity residual map (Fig. 9) shows an extended, blueshifted residual with an amplitude reaching -30 km s^{-1}, which is localized within the conical [O III] emission mapped in previous works. While it is likely that this residual is associated with the approaching side of the AGN bipolar outflow, it is possible that the adjacent redshifted residual, approximately centred at (1 arcsec, 0.5 arcsec), is due to the receding counterpart.

The BPT diagrams shown in Fig. 8 and the line ratio maps in Fig. 7 suggest that the residuals discussed above are located within, or adjacent to, a region dominated by AGN photoionization. However, to reach a definitive conclusion it is necessary to obtain spatially resolved, single-epoch observations of all emission lines used in the BPT diagrams (the [O III] and Hβ emission lines were not covered by our observation). The residual could be due to unresolved spectral features generated by the outflowing gas.

As already discussed in Section 3, visual inspection of the spectra revealed the presence of a line asymmetry, which we mapped by fitting GH polynomials to the emission lines (see Fig. 4). Blueshifted asymmetries are the spectral signatures expected to arise from outflowing gas moving towards the observer. It is therefore natural to ask whether they were observed in correspondence with the blueshifted residual. Unfortunately, the region where the extended blueshifted residual was identified could not be fitted with GH polynomials because of the presence of the broad Hα emission line.

The spatial distribution of the asymmetries is somewhat puzzling: the strongest blueshifted asymmetries are present over the entire right-hand side of the FOV (south-west and south-east of the nucleus), that is, in the receding side of the galaxy (see Fig. 1 or 10 to compare with near and far side of the galaxy). Conversely, mostly redshifted asymmetries, but with smaller amplitude than the blueshifted counterparts, are localized on the left side of the FOV (north-west and north-east of the nucleus). No evidence of significant asymmetries is recovered south-east of the nucleus, where the conical [O III] emission has been observed.

The velocity field associated with the asymmetry is also puzzling. With the goal of disentangling the rotating gas from the gas responsible for the asymmetry, we fitted the lines with two Gaussians. The velocity map for the component associated with the asymmetry is presented in the top panel of Fig. 5. With the exception of a few pixels, the right side of the FOV (south-west of the nucleus) is characterized by positive velocities with a Gaussian distribution of mean value approximately equal to 50 km s^{-1}. Conversely, the left side of the FOV, where only few pixels were fitted with two Gaussians, shows typical velocities of -25 km s^{-1}. There is no obvious relation with the presence of a biconical outflow.

As described in Section 4.3, we used the [S II] doublet to derive the electron density. Remarkably, Fig. 6 shows that a sharp increase in the electron density is spatially coincident with the fan-shaped blueshifted residual, a typical kinematical signature of outflows. In previous works, density enhancements have been observed in coincidence with kinematical features interpreted as due to outflowing gas (e.g. Holt et al. 2011; Schnorr-Müller et al. 2014a; Lena et al. 2015; Villar Martín et al. 2015). In their study of the narrow-line region of Mrk 477, Villar Martín et al. (2015) argue that the enhanced electron density associated with the outflow might be due to a shock induced by the radio jet. In the case of NGC 1365, this hypothesis is unlikely: first, as discussed below, there is little evidence of a radio jet; secondly, as shown by the BPT diagrams in Fig. 8, the line ratios 2 arcsec east of the nucleus are not characteristic of shock-induced ionization (i.e. LINER-like).

Downloaded from http://mnras.oxfordjournals.org/ at Universidade Federal do Rio Grande do Sul on October 26, 2016

The spatial coincidence between the density enhancement and the velocity residuals suggests a connection between the two: it is conceivable that the enhancement is due to a wind of denser gas, perhaps blown off the torus, and accelerated by the AGN radiation pressure (e.g. section 4 in Crenshaw et al. 2003, and references therein).

In previous works, non-circular motions in NGC 1365 have been mapped via the modelling of split line profiles in [O III] and other high-ionization species. Split lines are not resolved within our FOV, nevertheless from visual inspection of the data cube it is obvious that a second blueshifted component is present, in Hα, [N II] and [S II], in a handful of pixels near the edge of the FOV. More precisely, this region is characterized by (i) an enhancement in the velocity dispersion located around the point (4 arcsec, −3 arcsec), see middle panel in Fig. 3; (ii) by an evident decrease in the GH coefficient h_4, a proxy for the line kurtosis, indicating line profiles with a flat top, see bottom panel in Fig. 4. The same region has enhanced blueshifted velocity residuals as large as −27 km s^{-1} (see bottom panel in Fig. 9).

In summary, features suggestive of outflowing gas have been so far observed in high-ionization species. Here we found similar evidence also in a number of low-ionization species, i.e. [N II], Hα, [S II], and [O I]: we observed blueshifted velocity residuals in a fan-shaped region with the apex at the nucleus, oriented in the same way as the [O III] conical emission, with line ratios suggestive of AGN photoionization, and enhanced electron density; evidence for line splitting was identified in an adjacent area. A composite map of the spatial distributions of these features is presented in the bottom panel of Fig. 10.

Outflows can be powered by AGNs (e.g. Crenshaw et al. 2003; Veilleux, Cecil & Bland-Hawthorn 2005), star-formation activity (e.g. Axon & Taylor 1978; Veilleux & Rupke 2002), or a combination of the two (e.g. Cecil et al. 2001). If a radio jet is present, then it can influence the morphology and kinematics of the outflowing gas (e.g. Axon et al. 1998; Mazzalay et al. 2013). It has been suggested that NGC 1365 hosts a radio jet (Sandqvist, Joersaeter & Lindblad 1995). However, observations reported by Stevens et al. (1999) show that the bulk of the radio emission in the nuclear region is due to an elongated (8 × 20 arcsec^2) star-forming ring. The jet-like feature identified by Sandqvist et al. is seen to connect the nucleus to the ring, but if it is a jet, it is small and extremely weak. The galaxy is known to host both an AGN and intense star-formation activity. Therefore, it is natural to ask whether the outflow is predominantly powered by the AGN or by the star-forming regions. The wide-field IFU data obtained by Sharp & Bland-Hawthorn (2010) suggest that the outflowing gas is ionized by the AGN. Our data, which probe smaller scales at higher spatial resolution, provide supporting evidence that the AGN is powering the outflow: namely, the base of the velocity residual – which we interpret as a tracer of the outflow – is coincident with the unresolved nucleus. Therefore, the base of the outflow falls well inside the star-forming ring. Moreover, the presence of a broad Hα line, and the line ratios presented here, supports the hypothesis that the AGN is indeed the predominant ionizing source of the outflowing gas.

5.3 Is there any evidence for gas inflows?

Large-scale bars are among those dynamical features that funnel gas towards the inner region of their host galaxies. NGC 1365 has a strong bar with a projected major axis extending over about 200 arcsec (e.g. Zánmar Sánchez et al. 2008). Our observation, with an FOV of 13 × 6 arcsec^2 centred on the nucleus, probed only a very small fraction of the bar, in its central region. According to the hydrodynamical models of NGC 1365 presented in Lindblad et al. (1996b), this region falls entirely within the inner Lindblad resonance, which is located at a radius of $r \approx 30$ arcsec. Their model predicts the presence of spiral gas inflows within this region; however it must be acknowledged that it relies on a number of simplifying assumptions and, similarly to other studies (e.g. Zánmar Sánchez et al. 2008; Piñol-Ferrer, Lindblad & Fathi 2012), it attempts to reproduce the main features of the large-scale kinematics. The spatial resolution of the model is therefore not ideal for a direct comparison with our results.

The velocity residuals derived from the [N II] emission line do not show any obvious pattern which could be associated with gas inflows. It is worth recalling that a distinctive trait of the narrow emission lines is the presence of an asymmetric base. This is systematically blueshifted with respect to the line peak in the right-hand (south-western) portion of the FOV and redshifted in the left side. When the emission lines are modelled with two components, the asymmetry shows velocities which are lower than the velocities derived from the strongest spectral component, i.e. the narrow core (compare the velocity fields in Figs 3 and 5). Therefore, the asymmetric base could be tracing gas which is rotating more slowly than the gas responsible for the bulk of the line emission. In other words, it could originate from gas which lost angular momentum – perhaps via shocks along the edge of the large-scale bar – and it is slowly migrating from the inner Lindblad resonance towards the nucleus. In support of this speculation, we note that the observed region is embraced by two evident dust lanes (see top left panel in Fig. 1). These features are usually interpreted as tracers of gas which has been compressed, or shocked, at the leading edges of a bar (e.g. see section 6.5 in Binney & Tremaine 2008).

6 SUMMARY AND CONCLUSIONS

We observed the Seyfert 1.8 galaxy NGC 1365 using the GMOS integral field unit on the GEMINI South telescope. The FOV was centred on the nucleus and is aligned with the large-scale bar, covering 1173 × 541 pc^2. Our observation covered the spectral range 5600–7000 Å which includes a number of emission lines ([O I]λ6300, [N II]λλ6548,6583, Hα and [S II]λλ6716,6731). We modelled the profiles of these lines to produce velocity, velocity dispersion and flux maps with a spatial resolution of 52 pc and a spectral resolution of 49 km s^{-1}.

The flux maps are dominated by the strong and compact nuclear emission, while several bright knots, probably H II regions, are present elsewhere. The bright emission at the nucleus includes a prominent and unresolved broad component in the Hα emission line; because of the PSF wings, this contributes emission out to a radius of approximately 2 arcsec from the nucleus. The broad component was modelled with a combination of two Gaussians from which we derived a combined velocity dispersion of 1181 km s^{-1} and a flux-weighted velocity of −100 km s^{-1} (with respect to a systemic velocity of 1671 km s^{-1}, as derived from the [N II]λ6583 emission line).

Strong narrow emission lines are present over the entire FOV with velocity dispersion in the range 35–105 km s^{-1} and mean value $\sigma \approx 62$ km s^{-1}. The velocity fields derived from the [N II]λ6583 emission line and, independently, from Hα, [S II], and [O I] are consistent with gas rotating in the large-scale disc; however extended blueshifted velocity residuals suggest the presence of an additional kinematical component. The residual has a fan-shaped morphology with the apex at the nucleus; it is located within a region where

Downloaded from http://mnras.oxfordjournals.org/ at Universidade Federal do Rio Grande do Sul on October 26, 2016

previous authors observed an extended [O III] emission thought to trace a conical outflow (e.g. Storchi-Bergmann & Bonatto 1991); it corresponds to a sharp increase in the electron density (from 150 to 500 cm^{-3}), and it is characterized by line ratios typical of AGN photoionization ([N II]/H$\alpha > 0.6$). Close to this region we find evidence for line splitting. These features, previously observed at larger radii and for higher ionization species, are consistent with the hypothesis of a conical outflow suggested in previous works (e.g. Hjelm & Lindblad 1996). The presence of a broad Hα, the line ratios and the morphology of the velocity residuals support the hypothesis that the outflow is predominantly powered by the AGN.

Finally, although NGC 1365 shows overall morphological similarities with NGC 1097, we found no obvious evidence for gas inflows along nuclear spirals, like those observed in NGC 1097 by Fathi et al. (2006). However, the emission lines show a weak but evident asymmetry which is blueshifted with respect to the core of the lines in the right-hand side of the FOV, and redshifted in the left-hand side. This asymmetry could arise from gas which is rotating more slowly than the gas responsible for the bulk of the narrow-line emission. We speculate that it could be tracing gas which lost angular momentum, perhaps via the shocks traced by the adjacent prominent dust lanes, and it is now in the process of slowly migrating from the inner Lindblad resonance towards the nucleus of the galaxy.

ACKNOWLEDGEMENTS

We thank the anonymous referee for insightful comments, which helped us to improve the manuscript. DL acknowledges support from the National Science Foundation under grant no. AST-1108786 (PI Robinson), and from the European Research Council (ERC) under grant 647208 (PI Jonker). RAR acknowledges support from FAPERGS (project no. 2366-2551/14-0) and CNPq (project no. 470090/2013-8 and 302683/2013-5).

The authors wish to recognize and acknowledge the cultural role and reverence that the summit of Mauna Kea has always had within the indigenous Hawaiian community. We are most fortunate to have the opportunity to obtain data from observations conducted from this mountain. This work is based on observations obtained at the Gemini Observatory, which is operated by the Association of Universities for Research in Astronomy, Inc., under a cooperative agreement with the NSF on behalf of the Gemini partnership: the National Science Foundation (United States), the Science and Technology Facilities Council (United Kingdom), the National Research Council (Canada), CONICYT (Chile), the Australian Research Council (Australia), Ministerio da Ciencia e Tecnologia (Brazil) and southeast CYT (Argentina).

We acknowledge the usage of the HyperLeda data base (Makarov et al. 2014, http://leda.univ-lyon1.fr) and the NASA/IPAC Extragalactic Database (NED) which is operated by the Jet Propulsion Laboratory, California Institute of Technology, under contract with the National Aeronautics and Space Administration.

REFERENCES

Alexander D. M., Hickox R. C., 2012, New Astron. Rev., 56, 93
Allington-Smith J. et al., 2002, PASP, 114, 892
Alonso-Herrero A. et al., 2012, MNRAS, 425, 311
Athanassoula E., 1992, MNRAS, 259, 345
Axon D. J., Taylor K., 1978, Nature, 274, 37
Axon D. J., Marconi A., Capetti A., Macchetto F. D., Schreier E., Robinson A., 1998, ApJ, 496, L75
Baldwin J. A., Phillips M. M., Terlevich R., 1981, PASP, 93, 5
Barnes E. I., Sellwood J. A., 2003, AJ, 125, 1164
Beck R., Fletcher A., Shukurov A., Snodin A., Sokoloff D. D., Ehle M., Moss D., Shoutenkov V., 2005, A&A, 444, 739
Bekki K., 2000, ApJ, 545, 753
Bertola F., Bettoni D., Danziger J., Sadler E., Sparke L., de Zeeuw T., 1991, ApJ, 373, 369
Binney J., Tremaine S., 2008, Galactic Dynamics, 2nd edn. Princeton Univ. Press, Princeton
Braito V., Reeves J. N., Gofford J., Nardini E., Porquet D., Risaliti G., 2014, ApJ, 795, 87
Burbidge E. M., Burbidge G. R., 1960, ApJ, 132, 30
Burbidge E. M., Burbidge G. R., Prendergast K. H., 1962, ApJ, 136, 119
Cecil G., Bland-Hawthorn J., Veilleux S., Filippenko A. V., 2001, ApJ, 555, 338
Combes F. et al., 2014, A&A, 565, A97
Crenshaw D. M., Kraemer S. B., George I. M., 2003, ARA&A, 41, 117
Davies R. I. et al., 2014, ApJ, 792, 101
de Vaucouleurs G., de Vaucouleurs A., Corwin H. G., Jr, Buta R. J., Paturel G., Fouqué P., 1991, Third Reference Catalogue of Bright Galaxies. Volume I: Explanations and references. Volume II: Data for galaxies between 0^h and 12^h. Volume III: Data for galaxies between 12^h and 24^h. Springer, New York
Di Matteo T., Springel V., Hernquist L., 2005, Nature, 433, 604
Edmunds M. G., Pagel B. E. J., 1982, MNRAS, 198, 1089
Edmunds M. G., Taylor K., Turtle A. J., 1988, MNRAS, 234, 155
Emsellem E., Renaud F., Bournaud F., Elmegreen B., Combes F., Gabor J. M., 2015, MNRAS, 446, 2468
Fathi K., Storchi-Bergmann T., Riffel R. A., Winge C., Axon D. J., Robinson A., Capetti A., Marconi A., 2006, ApJ, 641, L25
Ferland G. J., Netzer H., 1983, ApJ, 264, 105
García-Burillo S., Combes F., 2012, J. Phys. Conf. Ser., 372, 012050
García-Burillo S., Combes F., Schinnerer E., Boone F., Hunt L. K., 2005, A&A, 441, 1011
Hjelm M., Lindblad P. O., 1996, A&A, 305, 727
Ho L. C., 2008, ARA&A, 46, 475
Holt J., Tadhunter C. N., Morganti R., Emonts B. H. C., 2011, MNRAS, 410, 1527
Hook I. M., Jørgensen I., Allington-Smith J. R., Davies R. L., Metcalfe N., Murowinski R. G., Crampton D., 2004, PASP, 116, 425
Hopkins P. F., Quataert E., 2010, MNRAS, 407, 1529
Iyomoto N., Makishima K., Fukazawa Y., Tashiro M., Ishisaki Y., 1997, PASJ, 49, 425
Jogee S., 2006, in Alloin D., ed., Lecture Notes in Physics. Physics of Active Galactic Nuclei at all Scales, Vol. 693. Springer Verlag, Berlin, p. 143
Jogee S., Kenney J. D. P., Smith B. J., 1999, ApJ, 526, 665
Jogee S., Baker A. J., Sakamoto K., Scoville N. Z., Kenney J. D. P., 2001, in Knapen J. H., Beckman J. E., Shlosman I., Mahoney T. J., eds, ASP Conf. Ser. Vol. 249, The Central Kiloparsec of Starbursts and AGN: The La Palma Connection. Astron. Soc. Pac., San Francisco, p. 612
Jones J. E., Jones B. J. T., 1980, MNRAS, 191, 685
Jorsater S., van Moorsel G. A., 1995, AJ, 110, 2037
Jorsater S., Lindblad P. O., Boksenberg A., 1984, A&A, 140, 288
Kewley L. J., Groves B., Kauffmann G., Heckman T., 2006, MNRAS, 372, 961
Knapen J. H., 2005, Ap&SS, 295, 85
Komossa S., Schulz H., 1998, A&A, 339, 345
Kristen H., Jorsater S., Lindblad P. O., Boksenberg A., 1997, A&A, 328, 483
Lena D., 2014, preprint (arXiv:1409.8264)
Lena D. et al., 2015, ApJ, 806, 84
Lindblad P. O., 1978, in Reiz A., Andersen T., eds, Astronomical Papers Dedicated to Bengt Stromgren. Copenhagen University Observatory, Copenhagen, p. 403
Lindblad P. O., 1999, A&AR, 9, 221
Lindblad P. O., Hjelm M., Hoegbom J., Joersaeter S., Lindblad P. A. B., Santos-Lleo M., 1996a, A&AS, 120, 403
Lindblad P. A. B., Lindblad P. O., Athanassoula E., 1996b, A&A, 313, 65

Downloaded from http://mnras.oxfordjournals.org/ at Universidade Federal do Rio Grande do Sul on October 26, 2016

Luo R., Hao L., Blanc G. A., Jogee S., van den Bosch R. C. E., Weinzirl T., 2016, preprint (arXiv:1603.07928)
Lynden-Bell D., 1969, Nature, 223, 690
Madore B. F. et al., 1999, ApJ, 515, 29
Markwardt C. B., 2009, in Bohlender D. A., Durand D., Dowler P., eds, ASP Conf. Ser. Vol. 411, Astronomical Data Analysis Software and Systems XVIII. Astron. Soc. Pac., San Francisco, p. 251
Mazzalay X., Rodríguez-Ardila A., Komossa S., McGregor P. J., 2013, MNRAS, 430, 2411
Makarov D., Prugniel P., Terekhova N., Courtois H., Vauglin I., 2014, A&A, 570, A13
Morgan W. W., 1958, PASP, 70, 364
Müller Sánchez F., Davies R. I., Genzel R., Tacconi L. J., Eisenhauer F., Hicks E. K. S., Friedrich S., Sternberg A., 2009, ApJ, 691, 749
Nardini E., Gofford J., Reeves J. N., Braito V., Risaliti G., Costa M., 2015, MNRAS, 453, 2558
Ondrechen M. P., van der Hulst J. M., 1989, ApJ, 342, 29
Ondrechen M. P., van der Hulst J. M., Hummel E., 1989, ApJ, 342, 39
Osterbrock D. E., Ferland G. J., 2006, Astrophysics of Gaseous Nebulae and Active Galactic Nuclei, 2nd edn. University Science Books, Sausalito, California
Pérez-Ramírez D., Knapen J. H., Peletier R. F., Laine S., Doyon R., Nadeau D., 2000, MNRAS, 317, 234
Peterson B. M., 1988, PASP, 100, 18
Phillips M. M., Frogel J. A., 1980, ApJ, 235, 761
Phillips M. M., Edmunds M. G., Pagel B. E. J., Turtle A. J., 1983, MNRAS, 203, 759
Piñol-Ferrer N., Lindblad P. O., Fathi K., 2012, MNRAS, 421, 1089
Riffel R. A., 2010, Ap&SS, 327, 239
Riffel R. A., Storchi-Bergmann T., Winge C., McGregor P. J., Beck T., Schmitt H., 2008, MNRAS, 385, 1129
Risaliti G., Elvis M., Fabbiano G., Baldi A., Zezas A., 2005, ApJ, 623, L93
Sandqvist A., Joersaeter S., Lindblad P. O., 1995, A&A, 295, 585
Scharwächter J. et al., 2015, preprint (arXiv:1507.01952)
Schnorr-Müller A., Storchi-Bergmann T., Riffel R. A., Ferrari F., Steiner J. E., Axon D. J., Robinson A., 2011, MNRAS, 413, 149
Schnorr-Müller A., Storchi-Bergmann T., Nagar N. M., Robinson A., Lena D., Riffel R. A., Couto G. S., 2014a, MNRAS, 437, 1708
Schnorr-Müller A., Storchi-Bergmann T., Nagar N. M., Ferrari F., 2014b, MNRAS, 438, 3322
Schulz H., Knake A., Schmidt-Kaler T., 1994, A&A, 288, 425
Schulz H., Komossa S., Schmitz C., Mücke A., 1999, A&A, 346, 764
Sharp R. G., Bland-Hawthorn J., 2010, ApJ, 711, 818
Shlosman I., Begelman M. C., Frank J., 1990, Nature, 345, 679
Smajić S., Moser L., Eckart A., Busch G., Combes F., García-Burillo S., Valencia S. M., Horrobin M., 2015, A&A, 583, A104
Soltan A., 1982, MNRAS, 200, 115
Steffen W., Koning N., Wenger S., Morisset C., Magnor M., 2011, IEEE Trans. Visual. Comput. Graphics, 17, 454
Stevens I. R., Forbes D. A., Norris R. P., 1999, MNRAS, 306, 479
Storchi-Bergmann T., Bonatto C. J., 1991, MNRAS, 250, 138
Storchi-Bergmann T., Dors Jr, O. L., Riffel R. A., Fathi K., Axon D. J., Robinson A., Marconi A., Östlin G., 2007, ApJ, 670, 959
van der Kruit P. C., Allen R. J., 1978, ARA&A, 16, 103
Veilleux S., Rupke D. S., 2002, ApJ, 565, L63
Veilleux S., Shopbell P. L., Rupke D. S., Bland-Hawthorn J., Cecil G., 2003, AJ, 126, 2185
Veilleux S., Cecil G., Bland-Hawthorn J., 2005, ARA&A, 43, 769
Veron P., Lindblad P. O., Zuiderwijk E. J., Veron M. P., Adam G., 1980, A&A, 87, 245
Véron-Cetty M.-P., Véron P., 2006, A&A, 455, 773
Villar Martín M., Bellocchi E., Stern J., Ramos Almeida C., Tadhunter C., González Delgado R., 2015, MNRAS, 454, 439
Zánmar Sánchez R., Sellwood J. A., Weiner B. J., Williams T. B., 2008, ApJ, 674, 797

This paper has been typeset from a TEX/LATEX file prepared by the author.

Downloaded from http://mnras.oxfordjournals.org/ at Universidade Federal do Rio Grande do Sul on October 26, 2016